JGR Space Physics

RESEARCH ARTICLE

Key Points:
- Flying over an area with no nearby lightning activity, the ASIM-MXGS instrument detected a 4 ms long event with a soft spectrum
- Observations coupled with simulations suggest that more than 90% of the counts come from a TEB and the rest from the associated TGF
- A source TGF with a broad angular distribution and 10^{17} to 10^{19} photons can explain the observation

The First Terrestrial Electron Beam Observed by the Atmosphere-Space Interactions Monitor

D. Sarria[1] , P. Kochkin[1] , N. Østgaard[1] , N. Lehtinen[1] , A. Mezentsev[1] ,
M. Marisaldi[1] , B. E. Carlson[1,2] , C. Maiorana[1] , K. Albrechtsen[1] , T. Neubert[3] ,
V. Reglero[4], K. Ullaland[1] , S. Yang[1], G. Genov[1], B. H. Qureshi[1], C. Budtz-Jørgensen[3],
I. Kuvvetli[3], F. Christiansen[3] , O. Chanrion[3] , M. Heumesser[3] , K. Dimitriadou[3],
J. Navarro-González[4] , P. Connell[4], and C. Eyles[4]

[1]Birkeland Centre for Space Science, University of Bergen, Bergen, Norway, [2]Physics and Astronomy, Carthage College, Kenosha, WI, USA, [3]National Space Institute, Technical University of Denmark, Lyngby, Denmark, [4]Astronomy and Space Science Group, University of Valencia, Valencia, Spain

Abstract We report the first Terrestrial Electron Beam detected by the Atmosphere-Space Interactions Monitor. It happened on 16 September 2018. The Atmosphere-Space Interactions Monitor Modular X and Gamma ray Sensor recorded a 2 ms long event, with a softer spectrum than typically recorded for Terrestrial Gamma ray Flashes (TGFs). The lightning discharge associated to this event was found in the World Wide Lightning Location Network data, close to the northern footpoint of the magnetic field line that intercepts the International Space Station location. Imaging from a GOES-R geostationary satellite shows that the source TGF was produced close to an overshooting top of a thunderstorm. Monte-Carlo simulations were performed to reproduce the observed light curve and energy spectrum. The event can be explained by the secondary electrons and positrons produced by the TGF (i.e., the Terrestrial Electron Beam), even if about 3.5% to 10% of the detected counts may be due to direct TGF photons. A source TGF with a Gaussian angular distribution with standard deviation between 20.6° and 29.8° was found to reproduce the measurement. Assuming an isotropic angular distribution within a cone, compatible half angles are between 30.6° and 41.9°, in agreement with previous studies. The number of required photons for the source TGF could be estimated for various assumption of the source (altitude of production and angular distribution) and is estimated between $10^{17.2}$ and $10^{18.9}$ photons, that is, compatible with the current consensus.

Plain Language Summary Terrestrial Gamma Ray Flashes (TGFs) are the highest energy natural particle acceleration phenomena occurring on Earth. They are burst of energetic photons associated with thunderstorms and have a poorly understood production mechanism. When interacting with the atmosphere, TGFs produce secondary electrons and positrons of high energy. A fraction of them can reach space and forms a beam under the effect of Earth's magnetic field, so called Terrestrial Electron Beam (TEB). They can be detected over geographical location with no lightning activity. In the past, most of the TEBs have been detected by the Fermi space telescope and the Compton Gamma ray Observatory. In this article, we report the first detection of a TEB by the Atmosphere-Space Interactions Monitor, docked on the International Space Station since April 2018. During this event, no lightning activity was detected below the instrument. The TEB's source lightning was actually found to be located 650 km away from detector, very close to an overshooting top of a thundercloud. The comparison of the observation with simulated data made it possible to constrain the geometry of the parent TGF. Our results point toward a relatively wide angular distribution and an intensity of $10^{17.2}$ to $10^{18.9}$ photons, in agreement with previous studies.

1. Introduction

Terrestrial Gamma ray Flashes (TGFs) are short (<2 ms) bursts of high energy (<30–40 MeV) photons, produced during thunderstorms, between 10 and 15 km altitude, for events detectable from space. A review of the science of TGFs is presented by Dwyer et al. (2012). TGFs were first detected using the BATSE experiment onboard the NASA's CGRO spacecraft (Fishman et al., 1994). Later, TGFs were recorded from space
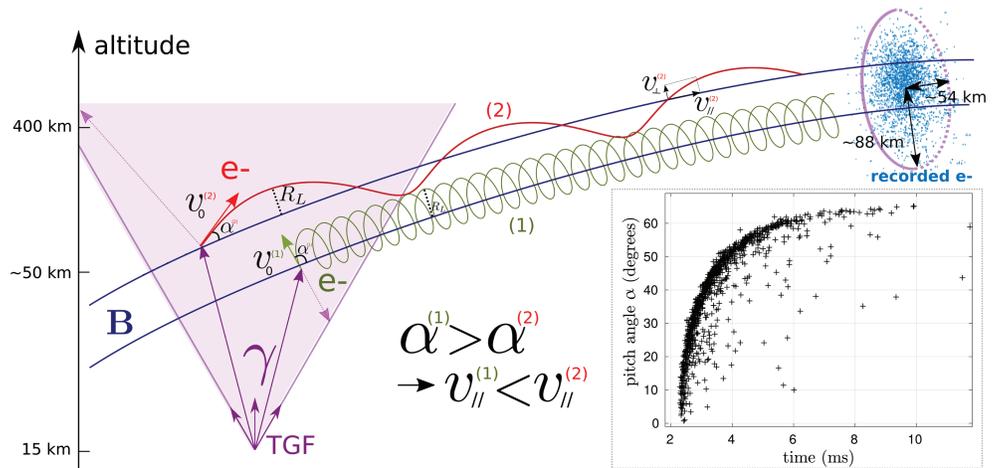
Figure 1. This sketch illustrates why the time distribution for a TEB event is mainly due to the pitch angle α with respect to Earth's magnetic field. Most of the electrons/positrons are relativistic and hence have a speed close to the speed of light. However, they have to follow helical trajectories around the field lines, and the electrons/positrons with larger α will undergo more rotations around the field lines, and with a larger Larmor radius (R_L) at the same electron energy, before reaching the satellite. They have actually a smaller velocity along the field line ($v_{//}$). More energetic electrons will have a larger R_L (as it is proportional to the Lorentz's γ factor). The insert shows the pitch angle as function of arrival time (according to the simulations described in section 4). At the satellite level, most of the electrons will arrive inside an ellipse of 54 km semiminor axis and 88 km semimajor axis.

by RHESSI (Smith et al., 2005), AGILE (MCAL instrument) (Marisaldi et al., 2014), the Fermi space telescope (GBM instrument) (Briggs et al., 2010; Roberts et al., 2018), BeppoSAX (Ursi et al., 2017), and the Atmosphere-Space Interactions Monitor (ASIM) (Neubert et al., 2019). ASIM is the only one specifically designed to detect TGFs from space, using the Modular X-ray and Gamma ray Sensor (MXGS) (Østgaard et al., 2019). ASIM was successfully launched and docked to the International Space Station (ISS) in April 2018 and started science operations in June 2018. The first results from ASIM are presented by Neubert et al. (2019) and Østgaard et al. (2019), in addition to this article.

TGFs deposit a large amount of energy in the atmosphere, as a large fraction (typically >97%) of the initial bremsstrahlung photons is absorbed before reaching space. By colliding with the atmosphere, the photons produce a large quantity of electrons (through Compton scattering and pair production) and positrons (pair production), but only a small fraction is able to escape the atmosphere. Most of the escaping electrons are produced above ≈40 km altitude (Sarria et al., 2015). Once they have escaped, the electrons and positrons are then bound to Earth's magnetic field lines and can travel large distances inside the magnetosphere (Briggs et al., 2011; Cohen et al., 2010; Dwyer et al., 2008). This phenomenon is called a Terrestrial Electron Beam (TEB). The TGF responsible for the TEB will be referred as the "source TGF" in the rest of this article. TEBs were first reported from measurements of the BATSE/CGRO spacecraft (Dwyer et al., 2008). Later, they were detected by the Fermi space telescope (Briggs et al., 2011), one event was found in the BeppoSAX satellite data archive (Ursi et al., 2017), and RHESSI also likely detected such an event (see Smith et al., 2006, and Gjesteland, 2012, Figure 4.6). The Fermi space telescope could also detect an event identified as both a TGF and a TEB (Stanbro et al., 2019). The duration of TEBs are several times longer that TGFs. This is because the electrons/positrons have a wide range of pitch angles (with respect to the local magnetic field direction) when they are produced and/or escape the atmosphere, which leads to a temporal dispersion after propagating several thousand of kilometers along Earth's magnetic field lines. This phenomenon is illustrated in Figure 1. For more information about the pitch angle distribution of TEB's electrons, see Sarria et al. (2016). A TEB typically contains 8% to 15% of positrons. All TGFs directed to space produce a TEB, but they are more difficult to detect than TGF. This is because a TGF can be detected by satellites located within a radius of about 800 km around its source, whereas TEBs extend only over a few tens of kilometers around the two point where the magnetic field line reaches the altitude of the satellite (in some cases, the apex of the magnetic field line is lower than the ISS altitude). For example, the first Fermi-GBM TGF catalog presents only 30 TEB candidates among the total of 4,135 listed TGF events (Roberts et al., 2018).

In this article we report the first TEB event detected by ASIM, using the MXGS instrument. Although the MXGS primary objective is to detect TGFs, a long trigger window (25 ms) was implemented to detect longer events like TEBs. In section 2, we present the ASIM-MXGS instrument and discuss its ability to detect TEBs. In section 3, we present the event detected on 16 September 2018. In section 4, we use Monte-Carlo simulation in order to reproduce the event and to constrain its beaming and its source content. We conclude in section 5.

2. Instruments and Data

The ASIM (Neubert et al., 2019) consists of two main instruments: MXGS for hard radiation observations and Modular Multispectral Imaging Array (MMIA) for optical observations (Chanrion et al., 2019). The MXGS instrument consists of a Low Energy Detector (LED) and a High Energy Detector (HED). Østgaard et al. (2019) described the instrument in details. The HED is based on 12 bismuth germanium oxide (BGO) scintillator crystal bars of $15 \times 5 \times 3.2$ cm^3 interfaced to photomultiplier tubes and is sensitive to energies of ~300 keV to ~40 MeV. It has a total geometrical area of 900 cm^2. The LED consists of an array of cadmium-zinc-telluride detector crystals with a total of 16,384 pixels and geometrical area of 1,024 cm^2. It operates in the energy range of ~70 to ~400 keV. The LED only operates during nighttime, and the event reported in this article happened during daytime. MXGS uses four trigger time windows: 300 μs, 1 ms, 3 ms, and 25 ms, this last being specifically implemented to target TEBs. For both detectors, if the recorded number of count exceeds a given threshold within one of these time windows, the MXGS instrument triggers and saves high-resolution data of every single recorded count inside a time frame of approximately ±1 s around the trigger time.

ASIM is mounted to the Columbus module on the ISS since April 2018. The ISS has been designed to always show the same side to the Earth, meaning that MXGS is always pointing toward the nadir. Let θ be the angle, measured from the ISS, between the nadir and the location of a TGF. All TGF events are expected to come with $\theta < 70°$. TEB's electrons and positrons are bounded to Earth's magnetic field lines and perform helical motion around it and therefore can hit the space station from any angle of incidence.

In order to simulate the response of MXGS to TGF and TEB, we developed a complete mass model of the instrument (Østgaard et al., 2019), based on the Geant4 toolkit (Agostinelli et al., 2003; Allison et al., 2006, 2016). It includes all relevant elements around the instrument, in particular the HED, LED, coded mask, shielding and electronics, MMIA, mounting platform, the other mounted instruments, and the Columbus module. By Monte-Carlo simulations, we estimated that the effective area of the HED for a typical TEB is about 150 cm^2, which is about 25% of the one for a typical TGF. In this case the effective area is calculated as the geometrical area ($\approx$900 cm^2 for HED and $\approx$1,024 cm^2 for LED) multiplied by the probability of an incident TEB electron to deposit more than 400 keV into at least one BGO crystal. This energy deposition can be direct (electrons/positrons hitting the crystal) or indirect. In the indirect case, electrons/positrons emit bremsstrahlung photons by interaction with the surrounding material that hit at least one BGO crystal. Each positron can also be affected by the annihilation process that takes place at the end of each track, when the kinetic energy goes down to zero. For HED, the indirect processes are mostly involved during TEB events, because of the shielding around the crystals stops most of the electrons/positrons. The effective area is a function of the energy of the electrons and positrons, and the value given previously is an average over a typical TEB spectrum. In addition to HED, we also estimated that the effective area of the LED detector for TEB detection is about 280 cm^2. It is significantly larger than for HED because direct electron hits are much more likely. It implies that, during a TEB event, the LED could detect twice more particles than the HED. This prediction should be testable with future events, since the LED was not operating for the event reported here.

3. Observation

ASIM-MXGS recorded an unusually long event on 16 September 2018, at 13:14:44.733601 (UTC). The event was strong enough to have been triggered by the 3 ms window. The recorded light curve is presented in Figure 2. The event consists of a pulse of more than 2 ms duration. Figure 3a shows the geometry of the event on a map. Table 1 gives a summary of the coordinates and times of the interesting points.

The data from World Wide Lightning Location Network (WWLLN) were also used for this analysis. It provides lightning timing and location by the use of a network of VLF sensors positioned on the ground around
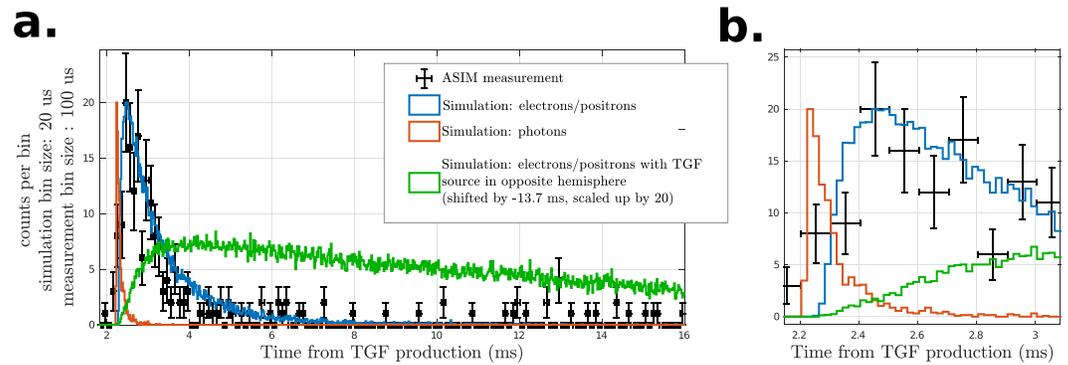
Figure 2. (a) Comparison between simulated and measured light curves for the TEB event. Error bars indicate a 1-σ interval and are calculated as the square root of the number of counts in each bin. Time 0 is when the source TGF is produced. The signals of the photons (TGF) and electrons/positrons (TEB) are shown. The simulated photon light curve (red) is scaled to have its maximum (that is located around 2.2 ms) at the same level as the maximum of the electron/positron light curve (blue). The observed light curve matches the electron/positron component (TEB) of 16 September 2018. The green histogram presents the TEB light curve that would be observed if the associated TGF was produced in the southern footpoint of the magnetic field line and shows a signal about 5 times longer that the observation. It was scaled in amplitude by a factor of 20 and shifted in time by -13.7 ms, to be able to display it inside the same time scale. (b) Zoomed in between 2.1 and 3.1 ms. The simulations indicate that photons from the TGF could also have been observed, and they should be mostly within the first 0.2 ms of the event. According to this simulation, most of the recorded counts below about 2.3 ms are due to photons.

the globe (Hutchins et al., 2012). According to WWLLN, there was no lightning activity below the ISS within a reasonable time window (few minutes) and distance (<600 km). We could estimate the position of the magnetic field line footpoint at 45 km altitude (approximately the altitude where most of the electrons that have a chance to escape the atmosphere are produced) in the northern hemisphere (see Table 1). This position was obtained from the model presented in Emmert et al. (2010), based on IGRF-12 (Thébault et al., 2015). These geographic coordinates were also confirmed by the two other codes, implementing the IGRF-12 model and a Runge-Kutta stepper to propagate the electrons/positrons along Earth's magnetic field (MC-PEPTITA and Geant4-based) that will be presented in section 4. Four WWLLN events were found around this location, within a time frame of less than 140 ms. Two of them are within 6 ms, well within the MXGS absolute timing uncertainty of about 20 ms. Since these two events happened within 0.1 ms and are close in location, they probably belong to the same flash. The coordinates of the events are given in Table 1, as Events 3 and 4. They are, respectively, 13.79 and 12.69 km away from the northern magnetic field line footpoint at 45 km altitude, knowing that the WWLLN has a generic positioning uncertainty of ±15 km. The probability of having a WWLLN event in such a narrow time window and position by random chance is extremely low. Therefore, these two points are likely close to the location of a lightning flash associated with the TGF that generated the TEB that was recorded by MXGS. In addition, simulated data, presented in section 4, also indicate that the time between the TGF production and the first electron reaching the detector is about 2.3 ms, which is close to travel time at the speed of light along the magnetic field line.

As it has been observed previously (see, e.g., Briggs et al., 2011; Ursi et al., 2017), a TEB could, in principle, come from a source TGF located at the magnetic footpoint of the opposite hemisphere. For this event, it is located at $\lambda = -29.920°$ (latitude), $\phi = -101.044°$ (longitude). However, we could not find any WWLLN match near this point within a reasonable time frame. Furthermore, according to simulations, the observed TEB duration in this configuration should be substantially longer than the observation (discussed in next section).

Figure 3a shows an image of the thunderstorm system located around the north magnetic field line footpoint, obtained by the geostationary satellite GOES-16 and has 0.5 km spatial resolution (Advanced Baseline Imager band 2, visible red, centered at 0.64 µm). The image was taken around 13:15:30 (UTC), that is, about 45 s after the ASIM trigger. The positions of the three closeby WWLLN events are presented, and all are within 6 ms of the ASIM trigger time. They also appear close to an overshooting top of the thunderstorm system. Overshooting tops correspond to a region with high convective activity, with a high lightning activity in the vicinity; therefore, it is not surprising if this region of the cloud generated a TGF.
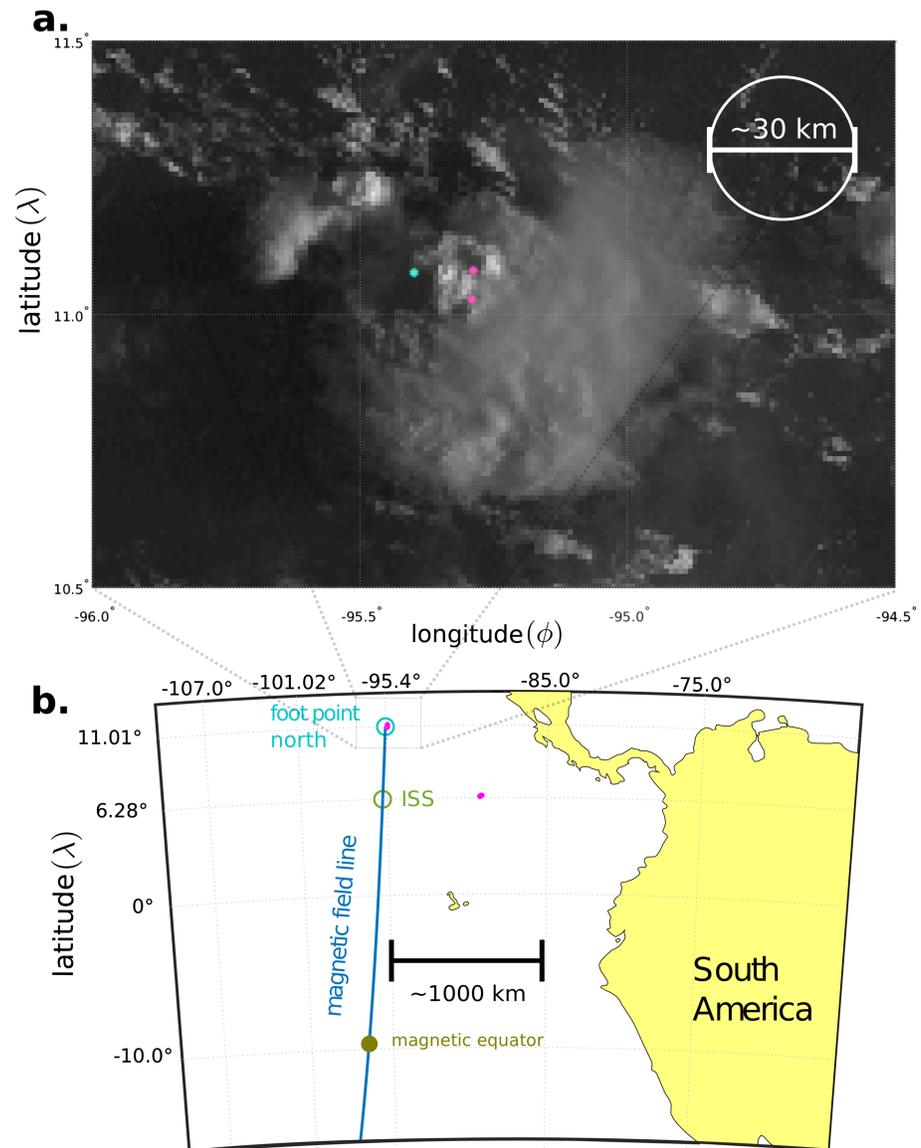
Figure 3. (a) Image from geostationary satellite GOES-16 on 16 September 2018, around 13:15:30 UTC (about 45 s after ASIM trigger time), zoomed around the north magnetic footpoint region. The image comes from the Advanced Baseline Imager instrument, Optical Band 2, centered at 0.64 µm, with 0.5 km resolution. The cyan dot gives the position of the footpoint at 45 km altitude of the magnetic field line intercepting the ISS location. The two closest positions obtained from WWLLN are presented as magenta dots that may correspond to a single discharge. They are within 6 ms of the ASIM trigger time (the MXGS absolute timing uncertainty is about 20 ms) and within 15 km of the northern magnetic footpoint (the WWLLN generic positioning uncertainty is ±15 km). The two points are located close to an overshooting top of the thunderstorm system. (b) The map shows the positions of interesting points of the event. The ISS (green dot) is located at a latitude $\lambda = 6.28°$ and a longitude $\phi = -95.71°$. The red dot is located at the northern magnetic footpoint of the magnetic field line passing though the ISS (coordinates $\lambda = 10.98°$, $\phi = -95.39°$). The corresponding magnetic latitude is 21.05° (modified apex). The small magenta dots are the position of the lightning discharges obtained from WWLLN sferic detections, within a time frame of 140 ms around the ASIM trigger time.

Since this event shows a relatively low flux (i.e., particle count rate), instrumental effects due to pulse pileup and dead time are weak. It was possible to correct for them and get reliable energy calibration and count rates. MXGS HED and LED data from the ASIM Science Data Center (in particular light curves and spectra) cannot be used for scientific analysis without performing mandatory postprocessing step (including instrumental effects corrections, calibration, and forward modeling using the Geant4 mass model), in collaboration with the ASIM-MXGS team. The energy spectrum of the event is presented in Figure 5. The

Table 1
Summary Table of the Time and Coordinates of the Interesting Elements for the ASIM Event That Happened on 16 September 2018

	Time (UTC)	λ (°)	ϕ (°)	h (km)	Δt (ms) (vr trg. time)	Δr (km) (vr mag. foot pt.)
Magnetic foot point	N.A.	11.076	−95.399	45		
International Space Station	13:14:44.733601	6.281	−95.709	402.5		
WWLLN event 1	13:14:44.601058	6.370	−89.376	N.A.	132.543	895.77
WWLLN event 2	13:14:44.700633	6.414	−89.301	N.A.	32.968	899.78
WWLLN event 3	13:14:44.738894	11.028	−95.291	N.A.	−5.293	13.79
WWLLN event 4	13:14:44.738925	11.081	−95.288	N.A.	−5.324	12.69

Note. All the given coordinates geodetic/geographic, using the WGS84 reference ellipsoid. WWLLN Events 3 and 4 are in a very narrow time (with respect to the event trigger time) and distance windows (with respect to the northern magnetic field line footpoint) and can be considered as good matches for the lightning discharge that produced the source TGF. Due to their very narrow time differences (<0.1 ms), these two matches probably belong to the same discharge. λ, ϕ, and h are latitude, longitude, and altitude.

spectrum is actually softer than what is recorded during usual TGF events. The inset in Figure 5 shows a zoom below 780 keV using a finer binning, which reveals a line around 511 keV. This line is broader than the ones detected by the Fermi space telescope (Briggs et al., 2011) due to different instrumental characteristics. A more detailed spectral analysis is presented in section 5.

4. Monte-Carlo Simulations of the Event

Numerical Monte-Carlo simulations were performed to reproduce the recorded light curves and energy spectrum of the event. Two models were used to propagate the TGF and secondary particles from the source of the TGF to ASIM: the MC-PEPTITA model (Sarria et al., 2015) and a new model based on the Geant4 toolkit (Agostinelli et al., 2003; Allison et al., 2006, 2016). The Geant4-based code is made publicly available (see Acknowledgments) and presented into more details in Appendix A. Both models are able to propagate photons, electrons, and positrons in Earth's environment, including the atmosphere and the Earth's magnetic field. They include the relevant processes for photons (Compton scattering, photoelectric absorption, pair production, and Rayleigh scattering) and electron/positron transport (elastic/inelastic scattering, bremsstrahlung, and annihilation). For simplicity, we only show results from the Geant4-based model, as both models showed very consistent results in all the simulations we performed.

The simulations start from a time instantaneous photon source, with a bremsstrahlung energy spectrum $\propto 1/\epsilon \times \exp(-\epsilon/7.3 \text{ MeV})$ (Dwyer et al., 2012). The TGF is located at 15 km altitude (later in this section, an altitude range between 10 and 16 km is tested), pointing toward zenith, with an opening angle that can be isotropic or Gaussian. The isotropic angular distribution is parameterized by the opening half angle θ and the Gaussian by the standard deviation σ_θ. The time reference is set to the source TGF production time, assumed to be located at the coordinates of the northern or southern magnetic footpoints. Figure 1 illustrates the geometry of the simulation and explains why TEBs are temporally more dispersed than TGFs and shows the pitch angle distribution as a function of arrival time that was obtained for this event. For a source TGF located at the north footpoint ($\lambda = 11.076°$, $\phi = -95.399°$), it takes about 2.28 ms for a direct photon (straight line) to travel from their source to the ISS (located about 650 km away), and the fastest electron/positron arrives about 48 μs later. The pointing angle between the ISS and the TGF source is about 58.4° with respect to nadir. The positron to electron ration of the TEB when it hits the ISS is about 13%. Simulated data indicate that 95% of the electron/positron beam is contained in an ellipse of semimajor axis of ≈88 km and semiminor axis of ≈54 km. For simplicity, we will consider in the following that the TEB is contained inside a circle, of about 70 km radius.

5. Discussion

Figure 2a presents a comparison between the observed light curve and the simulations. For all the simulations, except the green histogram, we assumed that the TGF was produced close to the northern footpoint of the magnetic field line that intercepts the ISS location. The simulated TEB light curve (electrons/positrons)
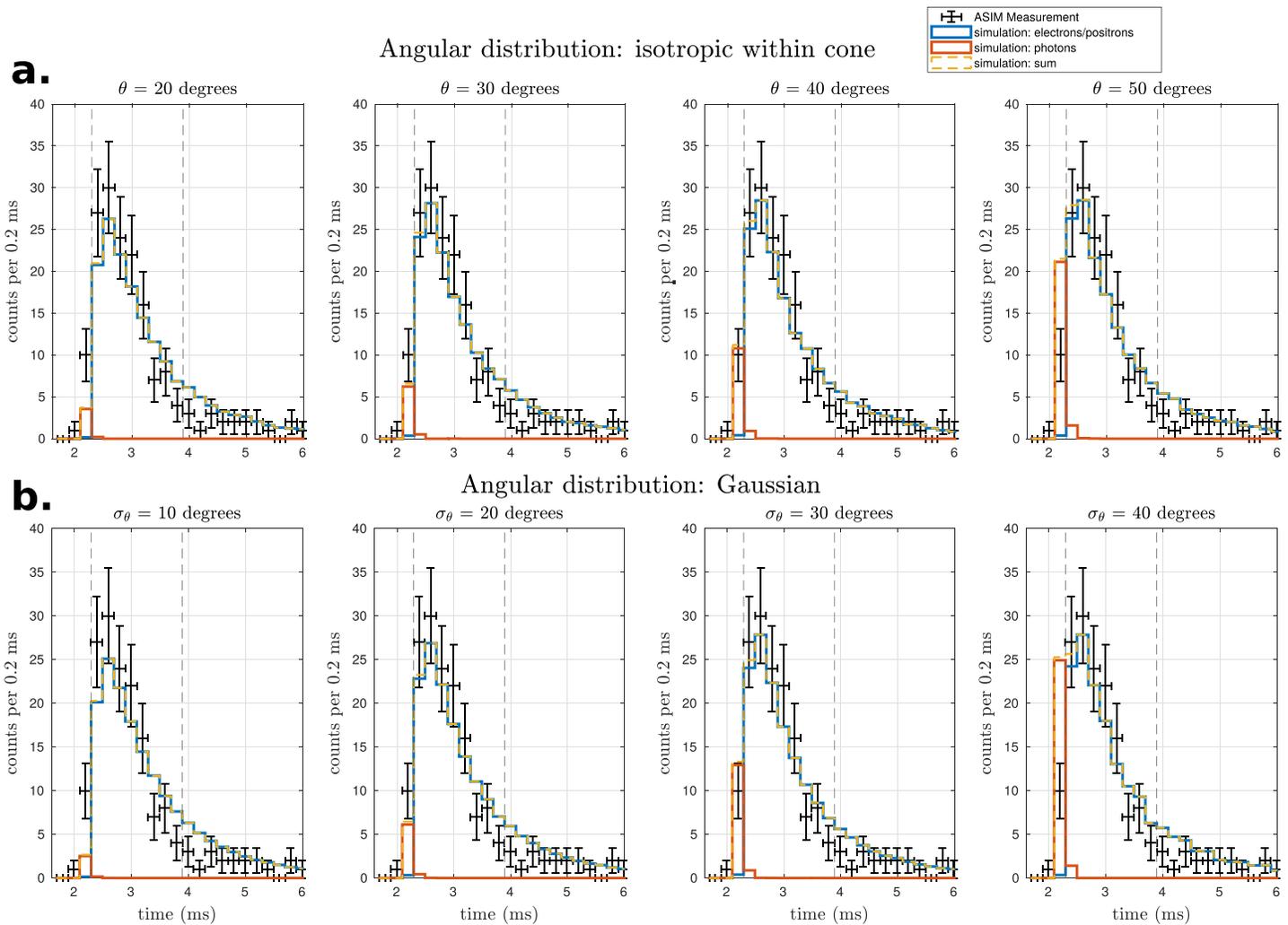
Figure 4. Comparison of the simulated and measured light curves, assuming various opening angles of the source TGF. Compared to Figure 2, the relative fluxes between electrons/positrons and photons take now into account the efficiency of the detector for the different particles. Error bars indicate a 1-σ interval and are calculated as the square root of the number of counts in each bin. The simulation is scaled to the measurement to minimize the value of the χ^2. The bins between 2.09 and 3.89 are used to compute it (shown with vertical dashed lines). A change in the source TGF opening angle mostly affects the photon (red) count rate between 2.09 and 2.29 ms. (a) Isotropic angular distribution inside a cone, with half angle θ. (b) Gaussian angular distribution with standard deviation σ_θ.

is compatible with the measurement. Here, the simulated photon light curve is arbitrarily scaled to have its maximum (that is located about 2.2 ms) at the same level as the maximum of the electron/positron light curve. The real relative amplitude between the two histograms is a function of the beaming angle of the source TGF and is discussed later.

TEB events may present a mirror pulse in some configurations. This is because charged particles moving in a converging magnetic field (i.e., a stronger field) are subject to the magnetic mirror "force" and are reflected. For this event, the IGRF-12 model gives a geomagnetic field magnitude at the northern footpoint (at 45 km altitude) of 34,590 nT and a weaker field of 29,949 nT (−13.4%) at the southern (i.e., opposite) footpoint; hence, no mirror pulse is expected. The light curve presented in Figure 2 does not present any mirror pulse indeed. There is a small count rate increase around 13 ms, that is consistent with background fluctuations. According to our calculation (time of travel along the field line), an hypothetical mirror pulse would be located much later, somewhere between 60 and 75 ms.

In principle, TEBs could be also detected when they are produced in the opposite hemisphere (i.e., the southern hemisphere in this case). In Figure 2a, the green histogram presents the light curve that would be observed if the TGF had been produced in the southern footpoint of the magnetic field line and shows
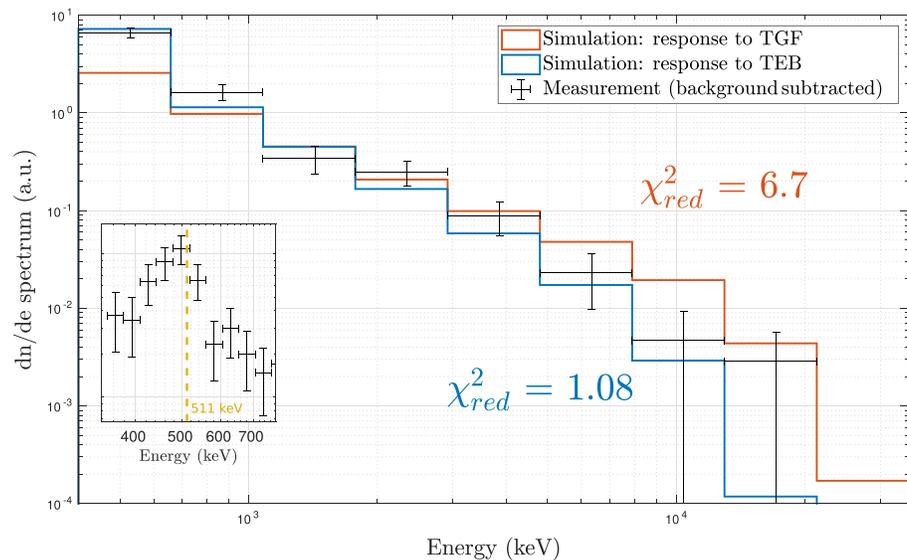
Figure 5. Energy spectrum comparison between the ASIM-MXGS measurement and simulations. The inset shows the recorded spectrum below 780 keV using a finer binning, which reveals a line around 511 keV. Two simulation scenarios were considered: Incoming particles are from TGF or TEB. The two simulated spectra are scaled to minimize the values of $\chi^2_{\rm red}$, and the minimum values obtained for each model are indicated.

a signal about 4 times longer that the observation ($\sim$20 ms compared to $\sim$5 ms). Figure 2b shows the same light curves as Figure 2a but zoomed-in between 2.1 and 3.1 ms. According to the simulation, the signal due to the photons from the TGF (produced $\approx$650 km away from the ISS) should be above the background level and have a t_{90} duration of about 150 μs, for photons above 400 keV (reminder: we assume, for now, an instantaneous TGF at source). The pulse due to TGF photons is about 20 times shorter than the one due to the TEB, that lasts about 5 ms. It indicates that some of the direct photons from the TGF may also have been detected. This fraction will depend on the location of the ISS with respect to the center of the electron/positron beam and, more importantly, on the angular distribution of the TGF.

Figures 4a and 4b present the same comparison as before but assuming several angular distributions for the source TGF. Compared to Figure 2, the relative effective areas of MXGS to detect photons ($\sim$650 cm^2) and electrons/positrons ($\sim$150 cm^2) are also taken into account. MXGS-HED is actually about 4.33 times more efficient to detect signal generated from incoming TGF photons than from TEB electrons and positrons. A change in the TGF angular distribution parameter mostly affects the counts inside the bin of the histogram located between 2.09 and 2.29 ms, containing mainly photons. A wider angular distribution of the source TGF implies that the relative amount of photons compared to electrons/positrons is increasing. A value of the angular parameter (θ or σ_θ) is considered compatible with the measurement if the photon (red) bin count between 2.09 and 2.29 ms lies inside the 1-σ error interval of the ASIM measurement in the same bin. For the isotropic (within a cone) angular distribution, the observed light curve is compatible with the simulations if a half angle of θ between 30.6° and 41.9° is used. For the Gaussian angular distribution, it is for a σ_θ between 20.6° and 29.8°. This range is in agreement with previous studies (Carlson et al., 2011; Dwyer & Smith, 2005; Hazelton et al., 2009; Mailyan et al., 2016; Østgaard et al., 2008). This scenario implies that about 3.5% to 10% of the recorded counts by ASIM-MXGS are actually direct TGF photons that arrive mostly at the beginning of the recorded light curve.

The previous results have been obtained assuming an instantaneously produced source TGF. But we also investigated the effects of using longer source TGF durations. We found that the constraint on the angular distribution is similar for any source duration $t^s_{90} < 197$ μs that corresponds to a recorded $t^d_{90} < 260$ μs after propagation to the satellite. It is probably the case, because according to the TGF duration distribution obtained from ASIM, $\approx$90% of the t_{90} durations are below 260 μs (Østgaard et al., 2019). For longer source durations, it is impossible to constraint the angular distribution using the method presented above. This discussion is presented in more detail in Appendix B.
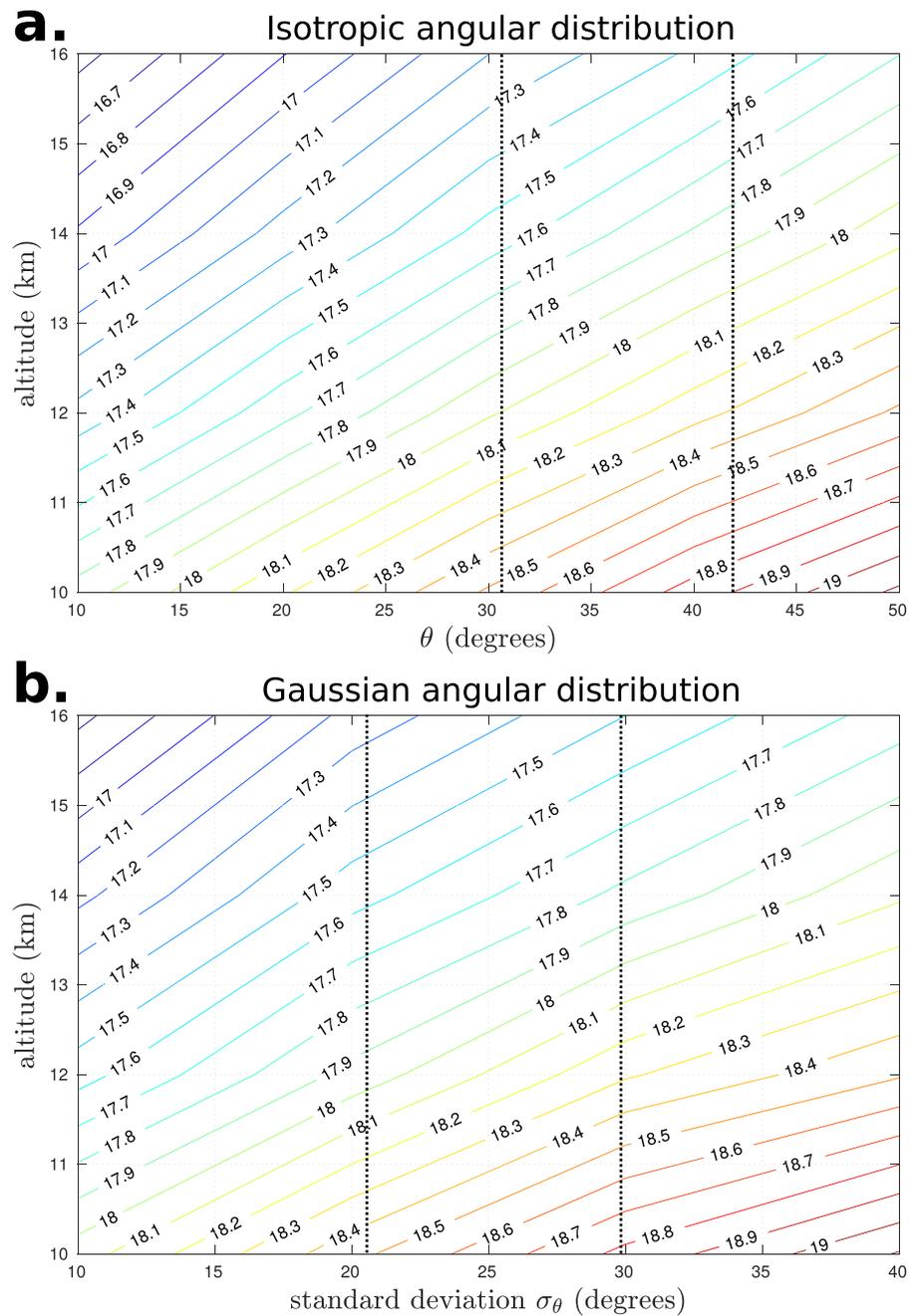
Figure 6. Level curves of the photon number intensity N_γ of the source TGF required for the simulation to produce the ≈160 counts recorded during the ASIM Event 180916. It is expressed as function of altitude and opening angle, in decimal logarithm. The dotted lines demarcate the parameter space where the angular distribution has been constrained (see Figure 4). (a) Assuming that the source TGF has a isotropic angular distribution inside a cone, with half angle θ. (b) Assuming a Gaussian angular distribution with standard deviation σ_θ.

Figure 5 presents a comparison between the recorded energy spectrum (background-subtracted) and simulations, using a strategy of forward modeling. Two scenarios are considered, one assuming that the incoming particles are photons from the TGF and the other assuming that the incoming particles are the secondary electron/positrons from the TEB. The TGF and TEB spectra are first calculated using the Geant4-based model of TGF propagation in the atmosphere with the assumptions presented previously (see section 4 and Appendix A). The particles are gathered at 400 km altitude, around the position of the ISS (±70 km). We verified that the TEB spectrum does not change significantly as a function of radial distance from its center

(the corresponding data and figures are presented in the associated data repository, see Acknowledgments). The results of this first simulation are then used as input for the ASIM Geant4 mass model (presented by Østgaard et al., 2019), and a set of simulated MXGS-HED spectra are produced. The quality of the simulated data compared to the observation can be quantified using the reduced chi squared (χ^2_{red}). The χ^2_{red} values obtained for the simulated response to a TGF and to a TEB are 7.2 and 1.13, respectively. Due to the chosen energy binning, there are 7 degrees of freedom, and using an usual 95% probability threshold, it gives a critical value $\chi^2_{red,c}$ equal to 2.01. It means that the TEB model, with $\chi^2_{red} < \chi^2_{red,c}$, is compatible with the measurement, whereas the TGF model, with $\chi^2_{red} > \chi^2_{red,c}$, is not. In addition to the results concerning the light curve (previous paragraph) and the geographical and time lightning matches (section 3), we think that it is enough evidence to consider that this event is mostly a TEB, with a small fraction (3.5% to 10%) of photons coming directly from the TGF.

Finally, we can estimate the required photons number N_γ of the source TGF in order to obtain the ≈160 counts that were observed by HED. The exact value of N_γ depends on assumptions of the source TGF, mainly the altitude of production and the angular distributions. We performed a series of simulation using the Geant4-based model, with a TGF altitude of production tested between 10 and 16 km, assuming an isotropic distribution of photons within a cone (with parameter the half angle of the cone, θ, tested from 10° to 50°), or a Gaussian distribution (with parameter the standard deviation σ_θ, tested from 10° to 40°). The results are presented in Figure 6.

The derived constraint on the TGF photon number is based on the number of electrons/positrons detected by ASIM-MXGS and not the number of photons as it is usually done. Most of the electrons/positrons that are detected by ASIM-MXGS are produced between 40 and 100 km altitude, along the Earth's magnetic field line that is intercepting the ISS location. Most of the electrons/positrons (>95% of the total number) are within 70 km radial distance around the field line. Widening the angular distribution of the source TGF will mostly increase the fraction of electrons produced far away from the magnetic field line (intercepting the ISS) and not reaching the ISS. In other words, increasing the value of the beaming angle mostly adds new photons that will not contribute to the TEB. Therefore, the dependence of N_γ on θ (when a source altitude is fixed) can be approximated as being proportional to the solid angle of a cone, that is, $N_\gamma(\theta) \propto \sin^2(\theta/2)$ (θ is a half angle). This was checked to fit quite accurately the profile of $N_\gamma(\theta)$, at a fixed source altitude. At a fixed opening angle, the variation of N_γ with altitude is directly linked to the absorption of the air. The absorption that has to be considered, that is, that will affect the number of produced electrons/positrons, is happening between the source altitude and about $h_l = 40$ km altitude. The integrated densities H that the TGF photons have to cross before reaching h_l are about 290.41, 215.60, 156.18, and 111.05 g/cm² for source TGFs at altitudes of 16, 14, 12, and 10 km, respectively. The photons get absorbed about 80.5 times more for a source at 10 km altitude, compared to a source at 16 km. This ratio is 14.0 for a source at 12 km altitude and 3.46 for a source at 14 km altitude. The profile of relative absorption can be obtained with $A(h) \propto exp(-H(h)\,\mu/\rho)$ and using an effective mass-energy absorption coefficient $\mu/\rho \approx 0.0247$ cm²/g. This value corresponds to the coefficient for air for photons at about 1.7 MeV, that is approximately the average of the assumed source TGF energy profile, if integrated between 60 keV and 40 MeV.

If the constraints on the angular distributions are considered (discussed before), a value of N_γ of $10^{17.2}$ (high altitude) up to $10^{18.9}$ photons (low altitude) is required to reproduce the particle count measured by ASIM-MXGS-HED (see Figure 6). This range is in agreement with values given by previous studies (Cummer et al., 2014; Dwyer & Smith, 2005; Dwyer et al., 2012; ?Gjesteland et al., 2015; Mailyan et al., 2016).

6. Conclusions and Future Work

We report the first TEB detected by the MXGS-HED instrument onboard the ASIM. It appeared as an unusually long event (>2 ms) with a spectrum softer than what is usually seen from TGF events. Tracing of the geomagnetic field line from the ISS permitted to estimate a likely geographical position of the TGF that produced the TEB, where three WWLLN matches within compatible time (<6 ms) and distance (<15 km) intervals were found. From geostationary imaging, obtained just about 45 s after the event, it appears that the TGF was produced in the vicinity of an overshooting top of a thunderstorm.

Using Monte-Carlo simulations to reproduce the observed light curve and energy spectrum, we show that the event is indeed mostly explained by a TEB, even if 3.5% to 10% of the detected flux may be direct TGF photons. A source TGF with a broad angular distribution can explain the observation ($\theta \approx 30.6$–41.9° for an
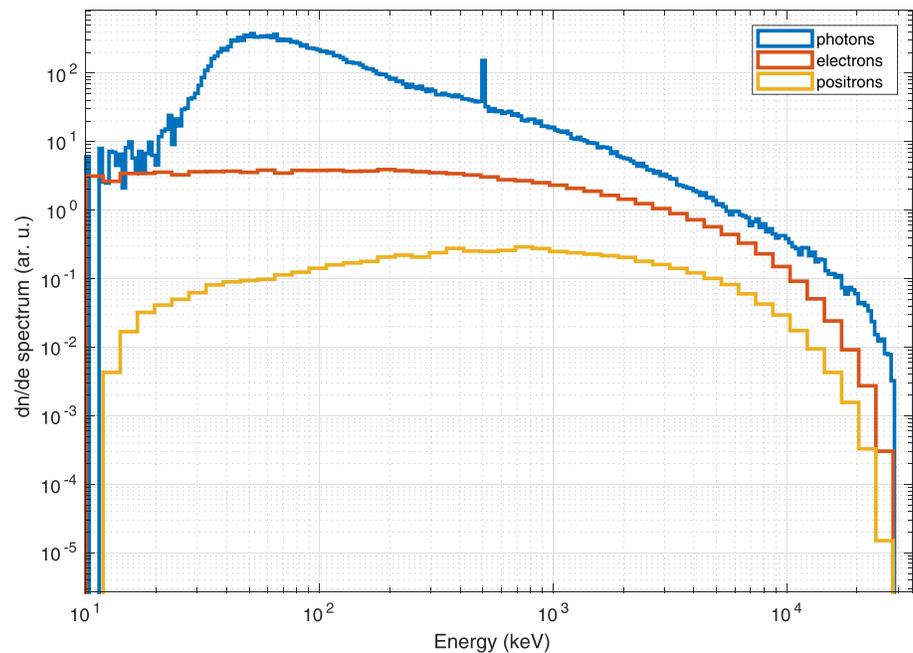
Figure A1. Results of the Geant4-based model simulation. Photon, electron, and positron energy spectrum, recorded at 400 km altitude, within 70 km radial distance around the ISS position (i.e., in a plane perpendicular to the local vertical). The photon spectrum uses a finer binning to better represent the 511 keV line when this spectrum is used as input for the ASIM mass model. The source TGF is located at 15 km altitude and has a Gaussian angular distribution centered toward zenith with standard deviation of $\sigma_\theta = 30°$. The amplitude of the spectra shown here is not representative of the fluence ratios (particles per cm^2) of the different particle types.

isotropic within cone distribution or $\sigma_\theta \approx 20.6$–$29.8°$ for a Gaussian distribution). This constraint is valid only if the source TGF has a duration $t_{90}^s < 197$ μs (which corresponds to a duration at satellite altitude of $t_{90}^s = 260$ μs). This is a likely possibility according to the distribution of TGF durations recorded by ASIM, where 90% of the TGFs have a $t_{90} < 260$ μs (see Østgaard et al., 2019, Figure 2). In addition, the intensity of the source TGF could be estimated for various assumptions of the source (altitude of production and angular distribution) and is between $10^{17.2}$ and $10^{18.9}$ photons. This range is in agreement with previous studies.

Here, we have discussed a TEB event detected during the daytime by the HED instrument alone. Future observations during nighttime have the added promise of simultaneous detection by the LED and MMIA instruments. It will allow measurements of the low-energy part of the spectrum (~70 to ~400 keV) and hypothetical UV and optical emissions associated with such events.

Planned for a launch in 2020, the TARANIS microsatellite (Lefeuvre et al., 2009) should also detect TEB events. It is primarily designed to detect both TGFs and TEBs, with help of the XGRE and IDEE instruments (Sarria et al., 2017), and will have, in addition, the capability of detecting hypothetical radio emissions from TEBs.

Appendix A: Geant4-Based Monte-Carlo Model of TGF and TEB Propagation in the Atmosphere, Ionosphere, and Magnetosphere

In order to estimate the response of MXGS-HED instrument for this event, we first needed to generate TGF (photons) and TEB (electrons and positrons) spectra just before they reach the ISS. We used a code based on the Geant4 toolkit (Agostinelli et al., 2003; Allison et al., 2006, 2016) to propagate particles in the atmosphere, ionosphere, and magnetosphere. The code is available in an online repository (see Acknowledgments). The geometry uses 256 exponentially spaced atmospheric layers between 1 and 150 km altitude (the atmosphere is negligible above) of constant density, composed only of N$_2$ and O$_2$, for simplicity and better performance. Densities within these layers are calculated with the NRLMSISE-00 model (Picone et al., 2002). The magnetic field of the Earth is modeled using the IGRF-12 model (Thébault et al., 2015). The propagation of photons, electrons, and positrons is simulated, including all the relevant processes, which are included in
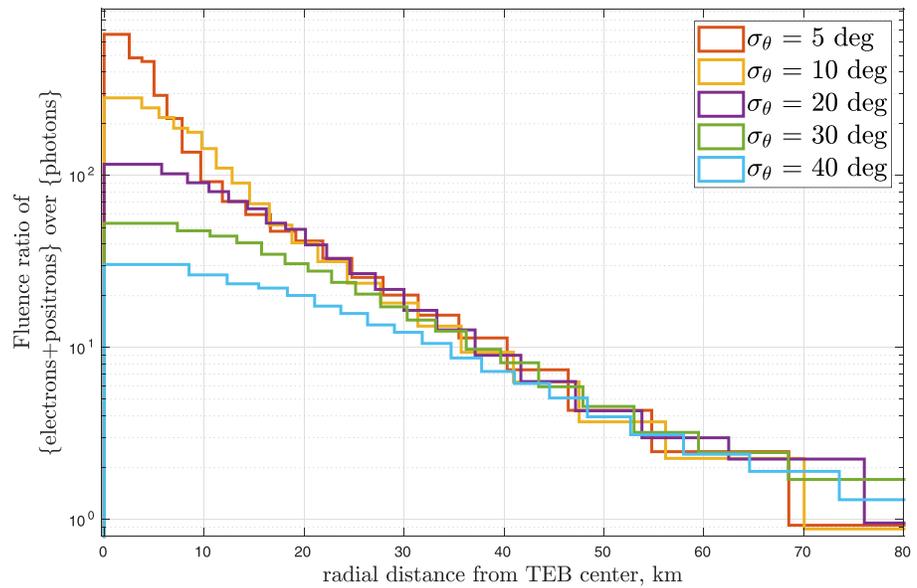
Figure A2. Fluence ratio between electrons + positrons (TEB) and photons (TGF) arriving at the ISS, according to the simulation. In this case, the ISS is located at about 650 km of the source TGF. The fluence ratio is presented as function of the distance between the ISS and the center of the electron beam, for several angular distributions (assuming a Gaussian distribution with parameter σ_θ). The source TGF is located at 15 km altitude. The response of the MXGS detector (i.e., the relative detection efficiency between electrons and photons) is not taken into account here. Note that the real spatial distribution of the leptons is contained inside an ellipse and here the particles are recorded inside rings (circular symmetry) for simplicity.

the Geant4 toolkit. Different models can be used (semianalytical or database driven like Livermore or Penelope), more-or-less accurate in the low energy part. In the context of photon/electron/positron propagation in air above 50 keV and without electric fields, they all show similar results as long as the effects of straggling are included (Rutjes et al., 2016), that is the default behavior of Geant4.

The source TGF is assumed to be a point source with adjustable altitude, typically set between 10 and 16 km. The energy spectrum has an exponential distribution proportional to $1/\epsilon \; \exp\left(-\epsilon/\epsilon_{cut}\right)$, with a cutoff $\epsilon_{cut} = 7.3$ MeV. The angular distribution is Gaussian with a standard deviation of 30° and has no tilt. The electrons, photons, and positrons are collected at an altitude of 400 km, inside a circle of $R = 80$ km radius around the position of the ISS. The spectra can be built using this data, but to properly build the photon light curve, R should be less than 1 km (to avoid artificial time broadening). Figure A1 shows the recorded energy spectra at 400 km altitude. They were then used as an input to calculate the response of the ASIM mass model to the TGF and the TEB. The electron energy spectrum can be fit by an exponential distributions ($\propto \exp\left(-\epsilon/\epsilon_{cutoff}\right)$, where ϵ is the energy). It results in cutoff energy of $\epsilon_{cutoff} = 2.88 \pm 0.176$ MeV that is compatible with the range of 2.3 to 4.6 MeV found by Briggs et al. (2011).

The amplitude of the spectra shown in the figure are not representative of the fluences (particles per cm²) of the different particle types. The fluence ratio of positions over electrons arriving to the ISS is about 13% in this case. For other settings of the source altitude or the angular distribution, it can fluctuate between 11% and 16%. The fluence ratio of electrons + positrons over photons arriving at the ISS is dependent on where the satellite is located with respect to the center of the TEB, on the offset between the TEB and the TGF (which depends on the geographical location) and on the angular distribution of the TGF. Figure A2 presents the evolution of this ratio as function of the distance to the center of the electron beam, for an initial TGF with a Gaussian angular distribution with several values of σ_θ.

Appendix B: Effect of Longer TGF Source Durations on the Angular Distribution Constraint

In this appendix, we provide a comprehensive discussion on the effects of assuming a longer TGF source duration (t_{90}^s) on the constraint on the angular distribution. If the TGF source duration is too long, it will blur
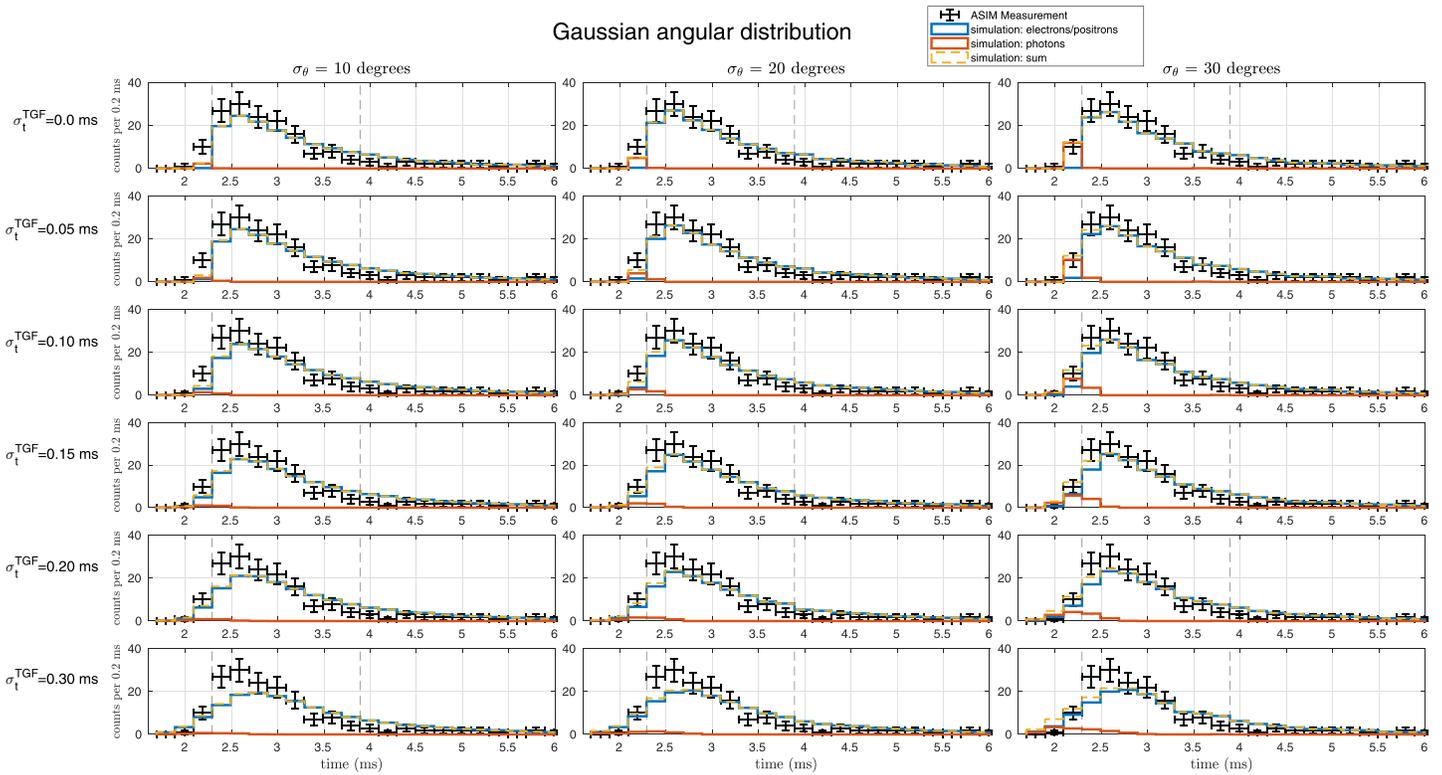
Figure B1. Comparison of the simulated (photons, electrons/positrons, and sum of both components) and measured light curves, assuming various opening angles and source duration of the source TGF. Error bars indicate a 1-σ interval and are calculated as the square root of the number of counts in each bin. The simulations are scaled to the measurement to minimize χ^2. The dashed vertical lines indicate the time interval (2.29 ms < t < 3.89 ms) where the χ^2 calculation is done (see Figure B2 for the results).

(or smear) both the detected TGF and the TEB light curves and could lead to different conclusions regarding the presented constraint on the beaming angle. We want to determine what is the maximum allowed value of t_{90}^d for the conclusions to be still valid.

First, it is important to distinguish between t_{90}^d, the detected TGF duration (when the TGF is detected by a satellite) and t_{90}^s, the source (or intrinsic, i.e., when the TGF is produced), because the propagation in the atmosphere implies a spread (or smearing) of the duration (and this spread is larger if the radial distance between the TGF source point and the subsatellite point is larger; it also depends on the considered photon energy range). We always have $t_{90}^d > t_{90}^s$. According to the simulation, assuming an instantaneous source ($t_{90}^s = 0$), the detected TGF t_{90}^d duration is about 150 μs in this case (the radial distance between the TGF source point and the subsatellite point is about 650 km). We can model the source TGF duration with a Gaussian (normal) distribution with parameter σ_t^{TGF}. Note that the t_{90}^s duration of the Gaussian time profile is directly linked to σ_t^{TGF} by $t_{90}^s = 3.290\,\sigma_t^{TGF}$ (and $t_{50}^s = 1.349\,\sigma_t^{TGF}$). For simplicity, we only show here the results for the Gaussian angular distribution.

Figure B1 presents how the light curves are changing with different σ_t^{TGF}. When σ_t^{TGF} is increased, the simulated light curves get too much smeared (spread out) compared to the measurement. This effect can be quantified by looking at the reduced χ^2 value between the simulation and the measurement. The value of χ_{red}^2 as function of σ_t^{TGF} is presented in Figure B2. Only the bins between 2.29 and 3.89 ms are kept for the χ^2 calculation (which are shown by the dashed vertical lines in Figure B1). An instantaneous TGF source ($\sigma_t^{TGF} = 0$) gives the best fit to the light curve, and increasing it gives less accurate ones. However, if we perform a χ^2 test, only σ_t^{TGF} values above 0.242 ms are rejected, using a standard 95% probability threshold.

In section 5, we established a constrain on the beaming angle by assuming that the beginning of the recorded light curve (i.e., the bin between 2.09 and 2.29 ms) contains mostly photons. This assumption will not be true anymore after increasing σ_t^{TGF} above a certain value. This is because increasing σ_t^{TGF} will smear both the photon and the electron/positron light curves (see Figure B1). Therefore, we must define a threshold
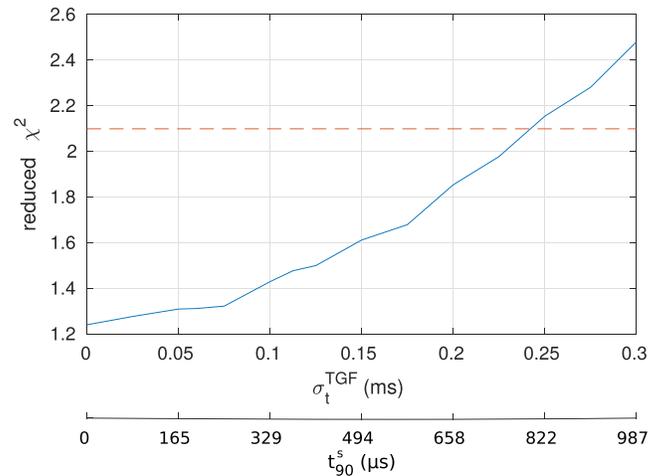
Figure B2. Reduced χ^2 between the simulated and the measured light curves, as function of the source duration of the TGF. The red vertical dashed line indicates the critical value ($\chi^2_{\mathrm{red,c}} = 2.1$).

for which we consider that the bin between 2.09 and 2.29 ms contains mostly photons. If we set it to 80% (i.e., 4 times more photons than electrons), then the maximum allowed σ_t^{TGF} is $\approx$60 μs. It corresponds to $t_{90}^s \approx$ 197 μs, and according to the simulation, the corresponding observed t_{90}^d should be about 260 μs (i.e., after propagating the TGF from the source at 15 km altitude to the satellite at $\approx$400 km altitude and at $\approx$650 km arc length distance). For any σ_t^{TGF} between 0 and 60 μs, the constraint on the angular distribution is about $21° < \sigma_\theta < 30°$, with small fluctuations with σ_t^{TGF}. For longer TGF source durations, it is not possible to establish a constraint on the angular distribution. The question is then how likely it is for the specific TGF that we are studying in this paper to have a $t_{90}^d < 260$ μs, as it is impossible to be sure about its real t_{90}^s. However, if we look into other TGF detection by ASIM and, more specifically, the distribution of observed TGF t_{90}^d durations (see Østgaard et al., 2019, Figure 2.B.), a large majority ($\approx$90%) are below $t_{90}^d = 260$ μs, with a most likely duration around $t_{90}^d = 75$ to 100 μs. It is therefore likely that the source TGF studied in this article has a t_{90}^d shorter than 260 μs.

References

Agostinelli, S., Allison, J., Amako, K., Apostolakis, J., Araujo, H., & Arce, P. (2003). GEANT4—A simulation toolkit. *Nuclear Instruments and Methods in Physics Research A*, *506*, 250–303. https://doi.org/10.1016/S0168-9002(03)01368-8

Allison, J., Amako, K., Apostolakis, J., Araujo, H., Dubois, P. A., & Asai, M. (2006). Geant4 developments and applications. *IEEE Transactions on Nuclear Science*, *53*, 270–278. https://doi.org/10.1109/TNS.2006.869826

Allison, J., Amako, K., Apostolakis, J., Arce, P., Asai, M., Aso, T., & Yoshida, H. (2016). Recent developments in GEANT4. *Nuclear Instruments and Methods in Physics Research A*, *835*, 186–225. https://doi.org/10.1016/j.nima.2016.06.125

Briggs, M. S., Connaughton, V., Wilson-Hodge, C., Preece, R. D., Fishman, G. J., Kippen, R. M., & Smith, D. M. (2011). Electron-positron beams from terrestrial lightning observed with Fermi GBM. *Geophysical Research Letters*, *38*, L02808. https://doi.org/10.1029/2010GL046259

Briggs, M. S., Fishman, G. J., Connaughton, V., Bhat, P. N., Paciesas, W. S., Preece, R. D., & Chekhtman, A. (2010). First results on terrestrial gamma ray flashes from the Fermi Gamma-ray Burst Monitor. *Journal of Geophysical Research*, *115*, A07323. https://doi.org/10.1029/2009JA015242

Carlson, B. E., Gjesteland, T., & Østgaard, N. (2011). Terrestrial gamma-ray flash electron beam geometry, fluence, and detection frequency. *Journal of Geophysical Research*, *116*, A11217. https://doi.org/10.1029/2011JA016812

Chanrion, O., Neubert, T., Lundgaard Rasmussen, I., Stoltze, C., Tcherniak, D., Jessen, N. C., & Lorenzen, M. (2019). The Modular Multispectral Imaging Array (MMIA) of the ASIM Payload on the International Space Station. *Space Science Reviews*, *215*, 28. https://doi.org/10.1007/s11214-019-0593-y

Cohen, M. B., Inan, U. S., Said, R. K., Briggs, M. S., Fishman, G. J., Connaughton, V., & Cummer, S. A. (2010). A lightning discharge producing a beam of relativistic electrons into space. *Geophysical Research Letters*, *37*, L18806. https://doi.org/10.1029/2010GL044481

Cummer, S. A., Briggs, M. S., Dwyer, J. R., Xiong, S., Connaughton, V., Fishman, G. J., & Solanki, R. (2014). The source altitude, electric current, and intrinsic brightness of terrestrial gamma ray flashes. *Geophysical Research Letters*, *41*, 8586–8593. https://doi.org/10.1002/2014GL062196

Dwyer, J. R., Grefenstette, B. W., & Smith, D. M. (2008). High-energy electron beams launched into space by thunderstorms. *Geophysical Research Letters*, *35*, L02815. https://doi.org/10.1029/2007GL032430

Dwyer, J. R., & Smith, D. M. (2005). A comparison between Monte Carlo simulations of runaway breakdown and terrestrial gamma-ray flash observations. *Geophysical Research Letters*, *32*, L22804. https://doi.org/10.1029/2005GL023848

Dwyer, J. R., Smith, D. M., & Cummer, S. A. (2012). High-energy atmospheric physics: Terrestrial gamma-ray flashes and related phenomena. *Space Science Reviews*, *173*, 133–196. https://doi.org/10.1007/s11214-012-9894-0

Emmert, J. T., Richmond, A. D., & Drob, D. P. (2010). A computationally compact representation of Magnetic-Apex and Quasi-Dipole coordinates with smooth base vectors. *Journal of Geophysical Research*, *115*, A08322. https://doi.org/10.1029/2010JA015326

Fishman, G. J., Bhat, P., Mallozzi, R., Horack, J., Koshut, T., & Kouveliotou, C. (1994). Discovery of intense gamma-ray flashes of atmospheric origin. *Science-AAAS-Weekly Paper Edition-including Guide to Scientific Information*, *264*(5163), 1313–1316.

Gjesteland, T. (2012). Properties of terrestrial gamma ray flashes. Modelling and analysis of BATSE and RHESSI data. The University of Bergen, http://bora.uib.no/handle/1956/6203

Gjesteland, T., Østgaard, N., Laviola, S., Miglietta, M. M., Arnone, E., Marisaldi, M., & Montanya, J. (2015). Observation of intrinsically bright terrestrial gamma ray flashes from the Mediterranean basin. *Journal of Geophysical Research: Atmospheres*, *120*, 12143–12156. https://doi.org/10.1002/2015JD023704

Hazelton, B. J., Grefenstette, B. W., Smith, D. M., Dwyer, J. R., Shao, X. M., Cummer, S. A., & Holzworth, R. H. (2009). Spectral dependence of terrestrial gamma-ray flashes on source distance. *Geophysical Research Letters*, *36*, L01108. https://doi.org/10.1029/2008GL035906

Hutchins, M. L., Holzworth, R. H., Brundell, J. B., & Rodger, C. J. (2012). Relative detection efficiency of the World Wide Lightning Location Network. *Radio Science*, *47*(6), RS6005. https://doi.org/10.1029/2012RS005049

Lefeuvre, F., Blanc, E., & Pinçon, J. L. (2009). TARANIS—A satellite project dedicated to the physics of TLEs and TGFs. In *American Institute of Physics Conference Series*, *1118*, pp. 3–7. https://doi.org/10.1063/1.3137711

Mailyan, B. G., Briggs, M. S., Cramer, E. S., Fitzpatrick, G., Roberts, O. J., Stanbro, M., & Dwyer, J. R. (2016). The spectroscopy of individual terrestrial gamma-ray flashes: Constraining the source properties. *Journal of Geophysical Research: Space Physics*, *121*, 11346–11363. https://doi.org/10.1002/2016JA022702

Marisaldi, M., Fuschino, F., Tavani, M., Dietrich, S., Price, C., Galli, M., & Vercellone, S. (2014). Properties of terrestrial gamma ray flashes detected by AGILE MCAL below 30 MeV. *Journal of Geophysical Research: Space Physics*, *119*, 1337–1355. https://doi.org/10.1002/2013JA019301

Neubert, T., Østgaard, N., Reglero, V., Blanc, E., Chanrion, O., Oxborrow, C. A., & Bhanderi, D. D. V. (2019). The ASIM mission on the International Space Station. *Space Science Reviews*, *215*(2), 26. https://doi.org/10.1007/s11214-019-0592-z

Neubert, T., Østgaard, N., Reglero, V., Chanrion, O., Heumesser, M., Dimitriaduo, K., & Eyles, C. J. (2019). A terrestrial gamma-ray flash and ionospheric UV emissions powered by lightning. *Science*. https://doi.org/10.1126/science.aax3872

Østgaard, N., Balling, J. E., Bjørnsen, T., Brauer, P., Budtz-Jørgensen, C., Bujwan, W., & Yang, S. (2019). *Space Science Reviews*, *215*, 23. https://doi.org/10.1007/s11214-018-0573-7

Østgaard, N., Gjesteland, T., Stadsnes, J., Connell, P. H., & Carlson, B. (2008). Production altitude and time delays of the terrestrial gamma flashes: Revisiting the burst and transient source experiment spectra. *Journal of Geophysical Research*, *113*, A02307. https://doi.org/10.1029/2007JA012618

Østgaard, N., Neubert, T., Reglero, V., Ullaland, K., Yang, S., Genov, G., Marisaldi, M., Mezentsev, A., Kochkin, P., Lehtinen, N., Sarria, D., Qureshi, B. H., Solberg, A., Maiorana, C., Budtz-Jørgensen, C., Kuvvetli, I., Christiansen, F., Chanrion, O., Heumesser, M., Navarro-Gonzales, J., Connell, P., Eyles, C., Christian, H., & Al Nussirat, S. (2019). First ten months of TGF observations by ASIM. *Journal of Geophysical Research: Atmospheres*. https://doi.org/10.1029/2019JD031214

Picone, J. M., Hedin, A. E., Drob, D. P., & Aikin, A. C. (2002). NRLMSISE-00 empirical model of the atmosphere: Statistical comparisons and scientific issues. *Journal of Geophysical Research*, *107*, 1468. https://doi.org/10.1029/2002JA009430

Roberts, O. J., Fitzpatrick, G., Stanbro, M., McBreen, S., Briggs, M. S., Holzworth, R. H., & Mailyan, B. G. (2018). The first Fermi-GBM terrestrial gamma ray flash catalog. *Journal of Geophysical Research: Space Physics*, *123*, 4381–4401. https://doi.org/10.1029/2017JA024837

Rutjes, C., Sarria, D., Broberg Skeltved, A., Luque, A., Diniz, G., Østgaard, N., & Ebert, U. (2016). Evaluation of Monte Carlo tools for high energy atmospheric physics. *Geoscientific Model Development*, *9*, 3961–3974. https://doi.org/10.5194/gmd-9-3961-2016

Sarria, D., Blelly, P. L., Briggs, M. S., & Forme, F. (2016). Studying the time histogram of a terrestrial electron beam detected from the opposite hemisphere of its associated TGF. *Journal of Geophysical Research: Space Physics*, *121*, 4698–4704. https://doi.org/10.1002/2015JA021881

Sarria, D., Blelly, P. L., & Forme, F. (2015). MC-PEPTITA: A Monte Carlo model for photon, electron and positron tracking in terrestrial atmosphere. Application for a terrestrial gamma ray flash. *Journal of Geophysical Research: Space Physics*, *120*, 3970–3986. https://doi.org/10.1002/2014JA020695

Sarria, D., Lebrun, F., Blelly, P. L., Chipaux, R., Laurent, P., Sauvaud, J. A., & Lindsey-Clark, M. (2017). *Geoscientific instrumentation, methods and data systems*, *6*, 239–256. https://doi.org/10.5194/gi-6-239-2017

Smith, D. M., Grefenstette, B. W., Splitt, M., Lazarus, S. M., Rassoul, H. K., Coleman, L. M., & Takahashi, Y. (2006). The anomalous terrestrial gamma-ray flash of 17 January 2004. AGU Fall Meeting Abstracts, AE31A-1040.

Smith, D. M., Lopez, L. I., Lin, R. P., & Barrington-Leigh, C. P. (2005). Terrestrial gamma-ray flashes observed up to 20 MeV. *Science*, *307*, 1085–1088. https://doi.org/10.1126/science.1107466

Stanbro, M., Briggs, M., Roberts, O., Cramer, E., Dwyer, J., Holzworth, R., & Xiong, S. (2019). A Fermi Gamma-ray Burst Monitor event observed as a terrestrial gamma-ray flash and terrestrial electron beam. *Journal of Geophysical Research: Space Physics*. https://doi.org/10.1029/2019JA026749

Thébault, E., Finlay, C. C., Beggan, C. D., Alken, P., Aubert, J., Barrois, O., & Zvereva, T. (2015). International Geomagnetic Reference Field: The 12th generation. *Earth, Planets, and Space*, *67*, 79. https://doi.org/10.1186/s40623-015-0228-9

Ursi, A., Guidorzi, C., Marisaldi, M., Sarria, D., & Frontera, F. (2017). Terrestrial gamma-ray flashes in the BeppoSAX data archive. *Journal of Atmospheric and Solar-Terrestrial Physics*, *156*, 50–56. https://doi.org/10.1016/j.jastp.2017.02.014

Erratum

In the originally published version of this article, some of the labels in Figure 2a were incorrect. The label for "Simulations: electrons/positrons" should have been for a blue plot (not a red plot) and the label for "Simulations: photons" should have been for a red plot (not a blue plot). This information was correct in the figure legend. The figure has since been updated and this version may be considered the authoritative version of record.